Reduced Graphene Oxide/MnO_2 Composite Films as the Electrodes for High-Performance Supercapacitors Produced by Successive Ionic Adsorption and Reaction (SILAR) Method

Vimuna V M[1,a] and Xavier T S[2,b]

[1] *Department of Physics, Dr. Palpu College of Arts and Science, University of Kerala, Kollam 691536, Kerala, India.*
[2] *Department of Physics, Government College for Women, University of Kerala, Thiruvananthapuram 695014, Kerala, India*

[a] vimunamurali@gmail.com
[b] xavierkattukulam@gmail.com

Abstract

In this work, rGO/MnO_2 (SL-GMN X) composites films on stainless steel (SS) substrate for three different number of cycles (X= 10, 15, and 20) has been prepared using the successive ionic adsorption and reaction (SILAR) method. This synthesis method provides a binder-free route. Fourier transform infrared spectroscopy (FTIR), X-ray photoelectron spectroscopy (XPS), and X-ray diffraction (XRD) were used to study the structure and composition of MnO_2 and SL-GMN X composite films. Transmission electron microscopy (TEM) and scanning electron microscopy (SEM) are used to assess the morphology of materials. Surface area and porosity measurements are analyze using Brunauer-Emmett-Teller analysis (BET). According to electrochemical investigations, when using a 1M Na_2SO_4 aqueous electrolyte in a three-electrode configuration, the SL-GMN 15 composite film exhibits an exceptional specific capacitance of 424 F g^{-1}. At a charging current of 1 mA, the SL-GMN 15 composite symmetric supercapacitor has a high specific capacitance of 117 F g^{-1} and a maximum energy density of 16.3 Wh kg^{-1}. Additionally, with a charging current of 3 mA, after 5000 cycles of testing, the composite has a long cycle life and retains a 99.5% specific capacitance. These findings pave the door for advancement of rGO/MnO_2 composite electrodes for supercapacitors and other energy storage applications.

Keywords: Successive ionic adsorption and reaction, Reduced graphene oxide, MnO_2, Symmetric supercapacitor.
Received 31 January 2025; First Review 21 February 2025; Accepted 22 February 2025

*** Address of correspondence**
Vimuna V M
Department of Physics, Dr. Palpu College of Arts and Science, University of Kerala, Kollam 691536, Kerala, India

Email: vimunamurali@gmail.com

How to cite this article
Vimuna V M and Xavier T S, Reduced Graphene Oxide/MnO_2 Composite Films as the Electrodes for High-Performance Supercapacitors Produced by Successive Ionic Adsorption and Reaction (SILAR) Method, J. Cond. Matt. 2024; 02 (02): 117-122.
Available from:
https://doi.org/10.61343/jcm.v2i02.137

Introduction

The growing need for efficient and eco-friendly energy storage technologies, including supercapacitors has generated a surge in demand in recent years due to rising traditional energy use [1-3]. Supercapacitors are gaining - wide acceptance due to their capacity to deliver increased power densities than batteries and better energy densities than electrostatic capacitors [4, 5]. Thermally reduced graphene oxide, which contains only a trace of oxygen, effectively enhances electronic conductivity, especially over long periods [6, 7].

The electrical conductivity and electrochemical characteristics of thermally reduced graphene oxide will be improved by providing a large surface for the deposition of nanoscale MnO_2 [8]. In the successive ionic adsorption and reaction (SILAR) method, the layer-by-layer formation of rGO and MnO_2 nanoparticles allow homogeneous spreading of MnO_2 on the rGO surface and terminate the agglomeration of rGO [9]. The morphology of different preparation processes will result in varying specific capacitance values.

In this chapter, the successive ionic adsorption and reaction (SILAR) method is used to prepare rGO/MnO_2 (SL-GMN) composites films on stainless steel (SS) substrate. This synthesis method provides a binder-free route. The rGO/MnO_2 coated directly onto the SS substrate has been used as a supercapacitor electrode. The unbalanced electrostatic force between SS and oxygen functionalities of rGO supports depositing rGO over SS substrate. This deposited rGO delivers anchoring sites to absorb Mn^{2+}, further oxidized to Mn^{4+}. The electrochemical and physical properties of the prepared films are thoroughly examined.

Method

As per our earlier research work, natural graphite powder was oxidize synthesize the rGO [10]. For two hours, 0.1053 g of prepared rGO was thoroughly dissolved in distilled water using ultrasonication. SS sheets are utilized as coating substrates. MnO_2/rGO composite thin films were coated on the flexible SS dipping in rGO dispersion. Here 5 beakers are used for coating MnO_2/rGO thin films. 80 ml rGO dispersion, 3M $MnSO_4$, and 2 M $KMnO_4$ were taken in the 1st, 3rd, and 4th beakers, respectively. The 2nd and 5th beakers contained double distilled water. The substrates were dipped into the beaker with precursor solution for 20 seconds in each solution and rinsed with double distilled water for 10 seconds. The substrate was dried for 5 seconds after retrieving from each beaker. This process is repeated for three cycles (10, 15, and 20), and we get three different MnO_2/rGO composite films (SL-GMN 10, SL-GMN 15, and SL-GMN 20). The weight of the SS substrate was taken before and after the coating to observe the mass of active material. For comparison, Pure MnO_2 film (SL-MN) was prepared using the same procedure without rGO.

X-ray diffraction (XRD), Fourier transform infrared spectroscopy (FTIR), energy dispersive X-ray analysis (EDAX), and X-ray photoelectron spectroscopy (XPS) were used to investigate the composition and structure of MnO_2 and SL-GMN X composites' films. Transmission electron microscopy (TEM) and scanning electron microscopy (SEM) are used to evaluate the morphology of materials. Brunauer-Emmett-Teller analysis is used to analyze porosity and surface area measurements (BET). More adsorption sites in SL-GMN 15 are made possible by large surface area and copious porosity, which shortens the ion diffusion pathway.

Analyses using cyclic voltammetry (CV) were conducted at different scan rates. With voltage amplitude of 10 mV, electrochemical impedance spectroscopy (EIS) measurements were made in the frequency range of 100 kHz to 100 Hz. An aqueous electrolyte solution containing 1M Na_2SO_4 was used for all studies. Using CV curves, the electrode materials' specific capacitance was determined using Equation (1) [11]:

$$Cs = \frac{\int IdV}{2mv\Delta V} \qquad (1)$$

The specific capacitance (Cs) of a symmetric supercapacitor can be computed from Equation (2) [11] using GCD curves:

$$Cs = \frac{2I\Delta t}{m\Delta V} \qquad (2)$$

The discharge voltage, discharge time, discharge current, and mass of the active material in one electrode are denoted by ΔV (V), Δt (s), I (A), and m (g), respectively. Equations. (3) and (4) [11] were used to measure the symmetric supercapacitor's specific energy (Es) and specific power (Ps):

$$Es = \frac{Cs\Delta V^2}{8} \qquad (3)$$

$$Ps = \frac{Es}{\Delta t} \qquad (4)$$

The specific power, specific energy, specific capacitance, discharge time, and potential window are denoted by Ps, Es, Cs, Δt and ΔV.

Discussions

The XRD results of the prepared rGO, SL-MN film, SL-GMN 10 composite film, SL-GMN 15 composite film, and SL-GMN 20 composite film were examined and are revealed in Figure 1(a). XRD patterns of rGO show two diffraction peaks at 25.8° and 43°, which can be indexed as the (002) and (100) reflections of graphene, respectively [12]. The broad diffraction peaks of all XRD peaks were related to low crystalline nature due to small grain size [13]. The diffraction patterns of the prepared SL-GMN 10, SL-GMN 15, and SL-GMN 20 composite films show peaks as in SL-MN, indicating that the crystal structure of MnO_2 nanoparticles is unaffected by the addition of rGO [14, 15].

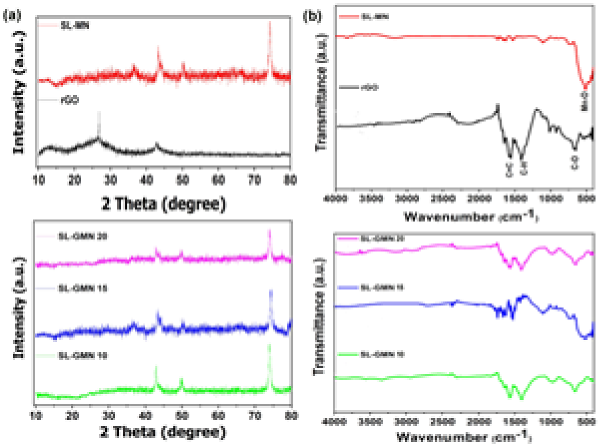

Figure 1: (a) XRD patterns and **(b)** FTIR spectra of rGO, SL-MN, SL-GMN 10 composite, SL-GMN 15 composite and SL-GMN 20 composite.

rGO, SL-MN, SL-GMN 10 composite, SL-GMN 15 composite, and SL-GMN 20 composite FTIR spectra are displayed in Figure 1b. The C-H stretching vibration is attributed to the peak at 1428 cm^{-1} [11]. Additionally, C=C stretching vibrations are responsible for the peak at 1625 cm^{-1} [16], while C-O stretching vibrations are responsible for the peak at 1107 cm^{-1} [17]. Mn-O stretching vibration is responsible for the distinctive peaks in SL-MN that are located between 570 and 450 cm^{-1} [18]. Both the rGO and MnO_2 bands are seen in the FTIR spectra of the SL-GMN

10, SL-GMN 15, and SL-GMN 20 composite, indicating that the MnO_2/rGO composite was successfully formed. Variations in temperature barely slightly alter the peak intensity.

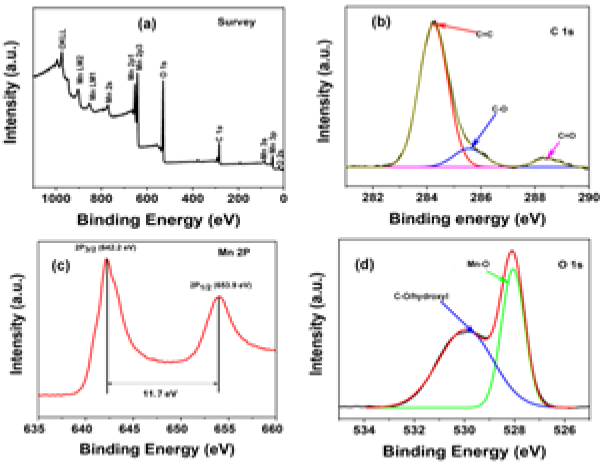

Figure 2: (a) XPS survey spectrum of SL-GMN 15 composite and its **(b)** C 1s **(c)** Mn 2p and **(d)** O 1s spectra.

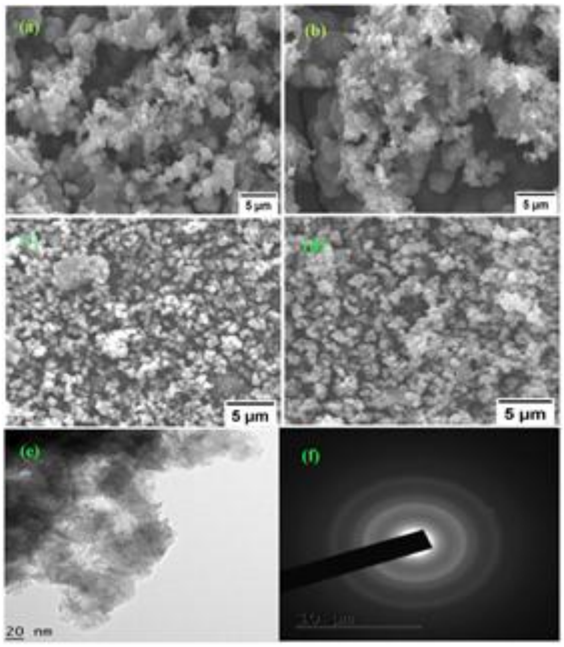

Figure 3: SEM images of (a) SL-MN, (b) SL-GMN 15 composite, (c) SL-GMN 10 composite, and (d) SL-GMN 20 composite. (e) TEM image of SL-GMN 15 composite (f) SAED pattern of SL-GMN 15 composite.

XPS was used to determine the surface composition and electronic state of the SL-GMN 15 composite, as shown in Figure 2. Figure 2a shows the composite's typical survey spectrum, which shows the presence of elements C, O, and Mn, implying the synthesis of MnO_2 on rGO. Three peaks at 284.4, 285.5, and 288.4 eV attributed to C=C, C-O, and C=O vibrations, respectively, in the high-resolution XPS range of C1s (Figure 2b) [19]. Mn $2P_{3/2}$ and Mn $2P_{1/2}$ are assigned to the peaks centred at 642.2 and 653.3 eV, respectively, according to the spectra of Mn 2P in Figure 2c. The energy difference between the Mn $2P_{3/2}$ and Mn $2P_{1/2}$ peaks is 11.7 eV, demonstrating that the composite is made up of MnO_2 [20]. In Figure 2d, the O1s core-level spectrum is displayed. Two Gaussian peaks appeared in the O1s spectra at 528.2 eV and 530 eV, respectively, and were attributed to Mn-O and C-O/hydroxyl [21].

SEM images demonstrating the morphology of the materials SL-MN, SL-GMN 15 composite, SL-GMN 10 composite, and SL-GMN 20 composite are seen in Figure 3. Figure 3a shows that SILAR coted SL-MN film consists of nearly spherical agglomerated nanoparticles. The SL-GMN 15 composite morphology (Figure 3b) shows that MnO_2 nanoparticles spread on the surface of rGO sheets. The SEM images of SL-GMN 10 composite and SL-GMN 20 composite are shown in Figure 3c and d, indicating less incorporating rGO with MnO_2 nanoparticles. The enhanced surface area of SL-GMN 15 composite increases the number of active sites in the electrochemical process.

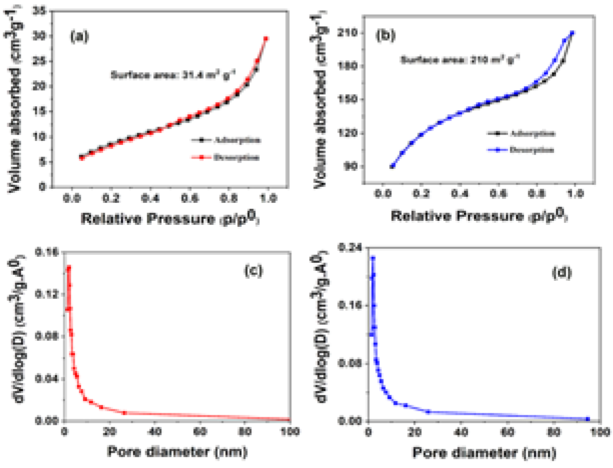

Figure 4: Nitrogen adsorption-desorption isotherm of (a) SL-MN, (b) SL-GMN 15 composite, and BJH pore-size distributions of (c) SL-MN, (d) SL-GMN 15 composite.

A High-resolution transmission electron microscope was used to assess the crystalline structure and morphology of the sample. HR-TEM micrograph of the SL-GMN 15 composite was shown in Figure 3e. The rGO surfaces were evenly coated with MnO_2 nanoparticles. The SL-GMN 15 composite's weak crystalline structure is demonstrated by the SAED pattern (Figure 3f). This outcome is in good agreement with the XRD findings.

Figures 4a and b display the nitrogen adsorption-desorption isotherms for the SL-MN and SL-GMN 15 composite, which were recorded. The SL-GMN 15 composite's nitrogen adsorption-desorption isotherms exhibit type-(IV) properties, confirming the composite's mesoporous structure. The SL-MN and SL-GMN 15 composites have BET surface areas of 31.4 m^2g^{-1} and 210 m^2g^{-1}, respectively. Because of its greater surface area, the SL-GMN 15 composite has a better absorption capacity. Figures 4c and d display the pore size distribution curve for the SL-MN and SL-GMN 15 composite, which was determined using the BJH method. For the SL-MN and SL-GMN 15 composite, the average pore size was 2 nm and 3.3 nm, respectively. The SL-GMN 15 composite's huge surface area and high mesoporous nature were thought to be caused by increased ionic transport through the material, which will improve the performance of the supercapacitor [22].

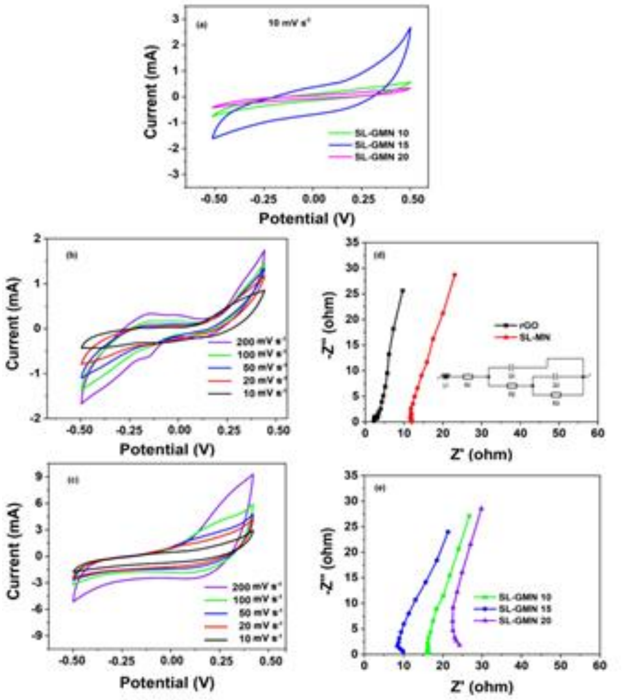

Figure 5: (a) CV curves of SL-GMN 10, SL-GMN 15, and SL-GMN 20 composite electrodes at the scan rate of 10 mVs^{-1}. **(b)** CV curves of SL-MN and **(c)** SL-GMN 15 composite electrodes in 1M Na_2SO_4 aqueous electrolyte solution in 1M Na_2SO_4 aqueous electrolyte solution with different scan rates. Nyquist plots of **(d)** rGO and (e) SL-MN, SL-GMN 10 composite, SL-GMN 15 composite, and SL-GMN 20 composite electrodes in 1M Na_2SO_4 aqueous electrolyte solution. Inset is an equivalent circuit diagram used for the fitting of the EIS data.

The electrochemical analysis of the prepared electrodes in a three-electrode system was usually established using CV and EIS. At a scan rate of 10 mVs^{-1}, the CV curves of the SL-GMN 10, SL-GMN 15, and SL-GMN 20 composite electrodes in the 1M Na_2SO_4 electrolyte under a potential range of -0.5 to 0.5 volts are shown in Figure 5a. Among them SL-GMN 15 composite electrode shows a larger area of CV curve, suggesting high specific capacitance.

In the 1M Na_2SO_4 electrolyte, the CV curves of the electrodes SL-MN and SL-GMN 15 composite at different scan speeds under a potential range of -0.5 to 0.5 volts are shown in Figure 5b and c. All figures show a minor distortion as the scan speeds increase, implying higher transport resistance due to polarisation. At a scan rate of 10 mVs^{-1}, the specific capacitance of SL-GMN 15 composite and SL-MN is 424 Fg^{-1} and 132 Fg^{-1}, respectively. At a scan rate of 10 mVs^{-1}, rGO has a maximum specific capacitance of 36.33 Fg^{-1} [23]. The vertical line in the lower-frequency range indicates optimal ion capacitive behaviour and minimal diffusion resistance in the electrode materials [24]. Figure 5d and e shows the Nyquist plots of the rGO, SL-MN, SL-GMN 10 composite, SL-GMN 15 composite, and SL-GMN 20 composite electrodes. The matching circuit diagram utilized in the EIS data fitting is shown in the Inset. In the high-frequency region, the resistance (Rs) of the SL-GMN 15 composite is 9.8 ohms, which is less than that of the SL-MN (3.5 ohms). With a more vertical line in the lower frequency band, the SL-GMN 15 composite electrode had the best capacitive performance of all the electrodes.

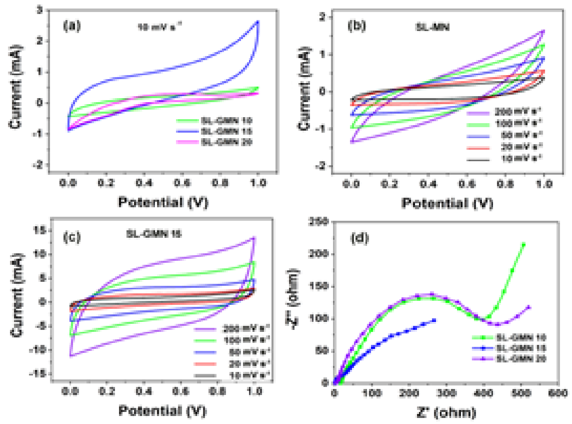

Figure 6: (a) CV curves of SL-GMN 10, SL-GMN 15, and SL-GMN 20 composite symmetric supercapacitors at the scan rate of 10 mVs^{-1}. CV curves of (b) SL-MN and (c) SL-GMN 15 composite symmetric supercapacitors at different scan rates. (d) Nyquist plots of SL-GMN 10, SL-GMN 15, and SL-GMN 20 composite symmetric supercapacitors.

CV, EIS, and GCD were used to examine the electrochemical performance of the symmetric supercapacitors SL-MN, SL-GMN 10 composite, SL-GMN 15 composite, and SL-GMN 20 composite. Figure 6a shows the CV curves of SL-GMN 10, SL-GMN 15, and SL-GMN 20 composite symmetric supercapacitors recorded at a scan rate of 10 mV s^{-1} and a cell voltage of 1 V. The area of CV curves is related to the specific capacitance. The integrated areas of the SL-GMN 15 composite symmetric supercapacitor CV curves are higher than those of the SL-GMN 10 and SL-GMN 20 composites, indicating that the SL-GMN 15 composite symmetric supercapacitor has good capacitance capabilities.

The CV curves of the SL-MN and SL-GMN 15 composite symmetric supercapacitors at scan rates varying from 10 to 200 mVs^{-1} in a cell voltage of 1 V are shown in Figure 6b and c. At a scan rate of 10 mVs^{-1}, the CV curve of the SL-GMN 15 composite symmetric supercapacitor showed a rectangular form. Due to its higher specific capacitance, the CV curves of the SL-GMN 15 composite symmetric supercapacitor show a wider area than those of the SL-MN for all scan rates.

As shown in Figure 6d, the EIS measured the impedance of SL-GMN 10, SL-GMN 15, and SL-GMN 20 composite symmetric supercapacitors. The charge transport resistance in the high-frequency field is represented by the semicircle. The lower Rct of SL-GMN 15 compared to SL-GMN 10 and SL-GMN 20 can be attributed to the composite symmetric supercapacitor's better electronic conductivity. The Warburg impedance arising from ion diffusion/transport in the electrolyte in the middle-frequency zone is shown by a straight line with a 45° slope. For the SL-GMN 15 composite symmetric supercapacitor, the discrepancy in the Warburg region shows excellent ion diffusion resistance.

To find out more about the composite electrodes' capacitive behaviour, galvanostatic charge-discharge tests were conducted. The charge-discharge curves of the composite symmetric supercapacitors SL-GMN 10, SL-GMN 15, and SL-GMN 20 were shown in Figure 7a with a constant charging current of 1 mA. Every charge-discharge curve exhibits symmetry. Equation (2) was used to calculate the specific capacitances. The specific capacitance for SL-GMN 10, SL-GMN 15, and SL-GMN 20 composite is 112, 469, and 102 Fg-1 at a current of 1 mA in two-electrode cell designs.

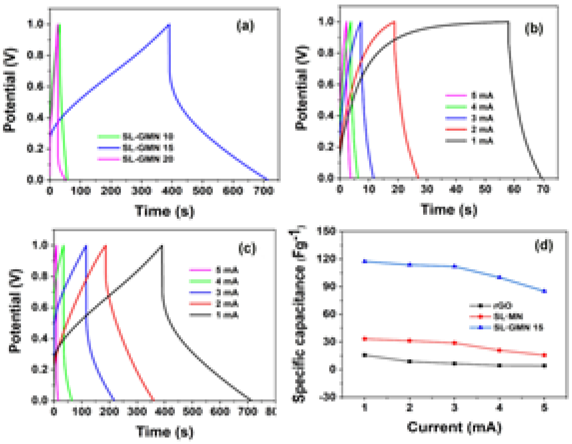

Figure 7: (a) GCD curves of SL-GMN 10, SL-GMN 15, and SL-GMN 20 composite symmetric supercapacitors at constant charging current 1 mA. GCD curves of (b) SL-MN and (c) SL-GMN 15 composite symmetric supercapacitors at at different charging currents. (d) Specific capacitance of rGO, SL-MN, and SL-GMN 15 composite symmetric supercapacitors at different charging currents.

Figure 7b and c display the galvanostatic charge-discharge curves of symmetric supercapacitors SL-MN and SL-GMN 15 composite at different currents ranging from 1 to 5 mA at a cell voltage of 1 V. All of the charge-discharge curves were symmetrical. At various currents of 1 mA, 2 mA, 3 mA, 4 mA, and 5 mA, the specific capacitances of SL-GMN 15 composite in a two-electrode symmetric arrangement are 469 Fg^{-1}, 455 Fg^{-1}, 448 Fg^{-1}, 400 Fg^{-1}, and 340 Fg^{-1}, respectively, are greater than that for SL-MN (133 Fg-1, 125 Fg^{-1}, 115 Fg^{-1}, 83.3 Fg^{-1}, 62.5 Fg^{-1}). The specific capacitance of the rGO symmetric supercapacitor is 9.1 Fg^{-1} at 1 mA [23]. SL-GMN 15 composite reached specific capacitance retention of 72% as the current increased from 1 to 5 mA, whereas SL-MN is only 46%. The specific capacitances of the rGO, SL-MN, SL-GMN 10 composite, SL-GMN 15 composite, and SL-GMN 20 composite at charging currents from 1mA to 5 mA were shown in Figure 7d.

Table 1: The electrochemical performances of some symmetrical supercapacitors in reported literatures and the present work.

Electrode	^aC_s (max) F g^{-1}	^bE_s (max) Wh kg^{-1}	^cT	^dC_m %$_T$	Ref
MnO_2/ reduced graphene oxide	152.5	…	1000	92	[24]
MnO_2/ reduced graphene oxide	342.8	…	3000	90.3	[25]
MnO_2/rGO composite	175	41.27	…	…	[26]
MnO_2/ reduced graphene oxide	343	…	2500	93.1	[27]
MnO_2/rGO	424	16.3	5000	99.5	This work

^aC_s (max), maximum specific capacitance,
^bE_s (max), maximum specific energy density,
^cT, cycles of cycle life test,
$^dC_m\%_T$, retention rate after the cycle life test.

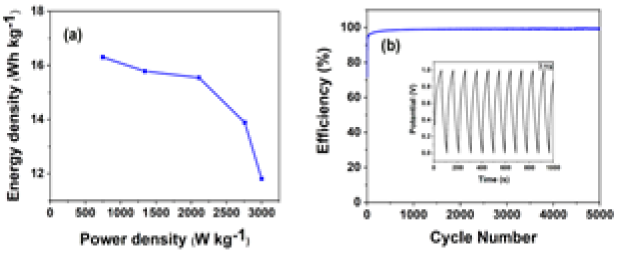

Figure 8: (a) Ragone plot of SL-GMN 15 symmetric supercapacitor. (b) Efficiency of SL-GMN 15 composite symmetric supercapacitor at a charging current of 3 mA and inset shows charge/discharge curves of the SL-GMN 15 composite symmetric supercapacitor in potential range from 0 to 1 V at a charging current of 3 mA.

Figure 8a shows the Ragone plot of the SL-GMN15 composite symmetric supercapacitor. The SL-GMN 15 symmetric supercapacitor's specific energy and power were computed at various currents ranging from 1 mA to 5 mA.

When specific power in 1M Na_2SO_4 increased from 784.4 to 3000 W kg^{-1}, the energy density decreased slightly. The result indicates that SL-GMN15 composite symmetric supercapacitor displayed a perfect power/energy combination.

The essential measure for assessing the supercapacitor device's performance is its cycle stability. Figure 8b displays the electrodes' long-term cyclic stability as determined by the galvanostatic charge-discharge curves at a current of 1 mA. With 99.5% of the initial capacitance still present after 5000 cycles, the SL-GMN 15 composite symmetric supercapacitor's specific capacitance demonstrated good cycling stability. The incorporation of thermally reduced graphene oxide during the composite production process is responsible for the exceptional cycling stability of our SL-GMN 15 composite symmetric supercapacitor. Table 1 displays a comparison between our SL-GMN 15 composite symmetric supercapacitor and other symmetric supercapacitors that have been described.

Conclusion

In summary, the binder free reduced graphene oxide/MnO_2 composite films were fabricated through a facile and controllable SILAR method. The small particle size and nearly amorphous condition are the causes of the broad peaks in all XRD patterns, which show poor crystalline nature. Both the rGO and MnO_2 bands are seen in the FTIR spectra of the SL-GMN 10, SL-GMN 15, and SL-GMN 20 composite, indicating that the MnO_2/rGO composite was successfully formed. The inclusion of MnO_2 and rGO is once again confirmed by the SEM pictures of the SL-GMN 15 composite, which show more porosity than SL-MN. Excellent specific capacitance of 424 F g^{-1} is demonstrated by the SL-GMN 15 composite electrode at a reduced scan rate (10 mV s^{-1}) and at a voltage range of 1V. The specific capacitance of the SL-GMN 15 composite symmetric cell is 117 F g^{-1} at a lower current of 1 mA. Furthermore, after 5000 cycles, the SL-GMN 15 composite symmetric supercapacitor's specific capacitance maintained 99.5% of its initial capacitance, demonstrating good cycling stability. For high-energy supercapacitors, this technique will thus offer a practical way to create binder-free MnO_2/rGO composite electrodes with a high specific capacitance.

References

1. Z Guo, H Zhang, K Liu, S Xie, L Zhang, X Fang, Y Xie, G Qin, J Yang, and Q Chen. Journal of Colloid and Interface Science, 2024.
2. Chaluvachar, Y N Priyanka, G T Sudhakar, Mahesha, G Vishnu Nair, Nakul Desai, and Dayananda K Pai, Journal of Energy Chemistry, 2024.
3. M Vandana, K Bijapur, G Soman, and G Hegde. Critical Reviews in Solid State and Materials Sciences, pp.335-370, 2024.
4. A A Mohamad, Inorganic Chemistry Communications, p.113677, 2024.
5. V K Kumar and N L Panwar, Journal of the Indian Chemical Society, p.101231, 2024.
6. V M Maphiri, G Rutavi, N F Sylla, S A Adewinbi, O Fasakin, and N Manyala, Nanomaterials, 11:8, 1909, 2021.
7. B Zhao, P Liu, Y Jiang, D Pan, H Tao, J Song, and W Xu, Journal of power sources, 198, 423-427, 2012.
8. Z Zhao, T Shen, Z Liu, Q Zhong, and Y Qin, Journal of Alloys and Compounds, 812, 152124, 2020.
9. M Jana, S Saha, P Samanta, N C Murmu, N H Kim, T Kuila, and J H Lee, Journal of Power Sources, 340, 380-392, 2017.
10. V M Vimuna, A. R Athira, K. D Babu, and T. S Xavier, Diamond and Related Materials, 110, 108129, 2020.
11. L Chen, H Yin, Y Zhang, and H Xie, Nano, 15(08), 2050099, 2020.
12. A Jabbar, G Yasin, W. Q Khan, M. Y Anwar, R. M Korai, M. N Nizam, and G Muhyodin, RSC advances, 7, 31100-31109, 2017.
13. H Huang, G Sun., J Hu, and T Jiao, Journal of Chemistry, 2015.
14. H Fei, N Saha, N Kazantseva, R Moucka, Q Cheng, and P Saha, Materials, 10, 1251, 2017.
15. S Chen, J Zhu, X Wu, Q Han and X Wang, ACS nano, 4, 2822-2830, 2010.
16. J Gao, H Li, M Li, G Wang, Y Long, Li, P, C Li and B Yang, Analytica Chimica Acta, 1145, 103-113, 2021.
17. F Raza, X Ni, J Wang, S Liu, Z Jiang, C Liu, H Chen, A Farooq and A Ju, Journal of Energy Storage, 30, 101467, 2020.
18. M Jayashree, M Parthibavarman, R BoopathiRaja, S Prabhu and R Ramesh, Journal of Materials Science: Materials in Electronics, 31, 2020.
19. J Mao, F F Wu, W H Shi, W X Liu, X L Xu, G F Cai, Y W Li and X H Cao, Chinese Journal of Polymer Science, 38, 514-521, 2020.
20. J Zhong, F Yi, A Gao, D Shu, Y Huang, Z Li, W Zhu, C He, T Meng and S Zhao, ChemElectroChem, 4, 1088-1094, 2017.
21. B Usharani, V Manivannan, and P Shanmuga sundaram, In Journal of Physics: Conference Series, 2070, 012089, IOP Publishing, 2021.
22. Y Liu, X Cai, B Luo, M Yan, J Jiang, and W Shi, Carbon, 107, 426-432, 2016.
23. V M Vimuna, B B Raj, S C Sam and T S. Xavier, Diamond and Related Materials, 120, 108707, 2021.

24. Y Xie and J Ji, Journal of Materials Research, 31, 1423-1432, 2016.
25. H Wang, Q Fu, and C Pan, Electrochimica Acta, 312, 11-21, 2019.
26. M Zhang, D Yang, and J Li, Vacuum, 178, 109455, 2020.
27. M Zhang, D Yang, and J Li, Journal of Energy Storage, 30, 101511, 2020.